Colloids and Surfaces A: Physicochemical and Engineering Aspects 743 (2026) 140587

Contents lists available at ScienceDirect

Colloids and Surfaces A: Physicochemical and Engineering Aspects

journal homepage: www.elsevier.com/locate/colsurfa

Comparative analysis of lateral and vertical microfluidic parallelization for high-throughput microdroplet generation

Lanting Xiang [a,b], Yu Zou [a,b], Yuanpeng Yu [a], Hazal Kutluk [a], Amina Moss [c], Iordania Constantinou [a,b,*]

[a] Institute of Microtechnology (IMT), Technische Universität Braunschweig, Alte Salzdahlumer Straße 203, Braunschweig, DE 38124, Germany
[b] Center of Pharmaceutical Engineering (PVZ), Technische Universität Braunschweig, Franz-Liszt-Str. 35a, Braunschweig, DE 38106, Germany
[c] Institute of Aquaculture, University of Stirling, Stirling, Scotland FK9 4LA, UK

GRAPHICAL ABSTRACT

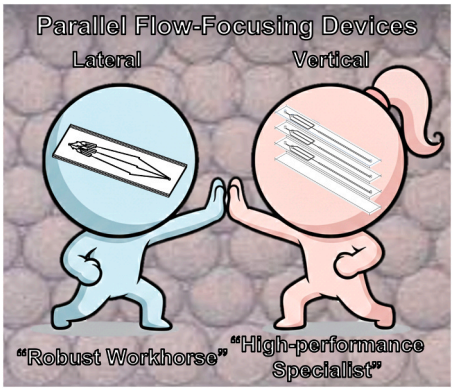

ARTICLE INFO

Keywords:
Droplet breakup
Interfacial dynamics
Flow-focusing microfluidics
Parallelized microfluidic systems
Capillary number scaling
Flow regime map
Geometric confinement
Scaling laws

ABSTRACT

The breakup of confined liquid threads in microfluidic flow-focusing geometries is governed by the interplay between interfacial tension, viscous stresses, and hydrodynamic resistance, which becomes increasingly complex in parallelized systems operated at high throughput. While parallelization is widely used to increase microdroplet generation rates, the role of architecture in regulating droplet breakup dynamics and inter-channel uniformity remains insufficiently understood. Here, we systematically compare microdroplet formation in lateral and vertical parallel flow-focusing architectures using glass microfluidic devices. By constructing flow regime maps and performing quantitative scaling analyses, we show that the two architectures exhibit markedly different droplet breakup behaviors, characterized by distinct scaling exponents for droplet size and generation frequency. These differences reflect geometry-dependent physical mechanisms governing the balance between interfacial tension, shear stress, and flow resistance during droplet formation. Furthermore, we demonstrate that geometric coupling in parallelized flow-focusing systems imposes contrasting constraints on flow redistribution among channels, leading to different limits in microdroplet size uniformity and attainable generation frequency.

* Corresponding author at: Institute of Microtechnology (IMT), Technische Universität Braunschweig, Alte Salzdahlumer Straße 203, Braunschweig, DE 38124, Germany.
E-mail address: i.constantinou@tu-braunschweig.de (I. Constantinou).

https://doi.org/10.1016/j.colsurfa.2026.140587
Received 5 February 2026; Received in revised form 14 April 2026; Accepted 17 April 2026
Available online 19 April 2026
0927-7757/© 2026 The Authors. Published by Elsevier B.V. This is an open access article under the CC BY license (http://creativecommons.org/licenses/by/4.0/).

The lateral architecture supports robust and uniform droplet breakup over a broad operational window, whereas the vertical architecture enables higher-frequency droplet generation but with increased sensitivity to flow imbalance. Together, these results establish a geometry–hydrodynamics framework linking device architecture to droplet breakup regimes and scaling behavior, providing predictive design principles and new fundamental insight into interfacial dynamics in parallelized microfluidic systems.

1. Introduction

Microfluidic devices are now widely recognized as indispensable tools in research and development, used to enable the precise control and manipulation of small fluid volumes in diverse applications, including drug delivery, diagnostics, chemical and biological synthesis [1–3]. Among the various microfluidic technologies, droplet-based microfluidics has emerged as a particularly powerful approach for biological and chemical screening and experimentation, offering picoliter- to nanoliter-scale droplets with high uniformity for efficient reagent compartmentalization and precise control of reactions and processes [4,5]. These features make microfluidic droplet generators highly attractive for applications such as single-cell analysis [6], enzyme screening [7], and the production of functional microcapsules for applications including carbon capture and thermal energy storage [8,9]. Increasing industrial interest in applying these processes is now motivating the push toward higher-throughput systems that support scale-up and automation [10]. Despite the motivation, throughput remains a significant limitation of most microfluidic droplet generating systems, as total droplet generation rates are often too low for technology adoption beyond research laboratories [11].

In a microfluidic droplet generator, microdroplet formation occurs when two immiscible fluids, referred to as the dispersed phase (forming microdroplets) and the continuous phase (shearing and transporting the microdroplets), meet under controlled flow conditions within a microchannel network. The breakup of the dispersed phase into discrete microdroplets is governed by the complex interplay between the shear forces exerted by the continuous phase onto the dispersed phase, the interfacial tension between the two fluids, the viscous and inertial forces related to fluid properties, and the geometry and dimensions of the microchannels [12]. The throughput of a single microdroplet generating unit (mDGU) is mainly determined by the geometry and dimensions of the microchannel, the properties of the used fluids and the operating parameters, such as the flow rates of the two phases. Studies comparing commonly used microfluidic droplet-generation strategies, such as co-flow, cross-flow (T- and Y-junctions), flow-focusing, and step emulsification, have shown that flow-focusing geometries provide the highest throughput while maintaining monodisperse microdroplet formation across a wide diameter range (10–1000 μm) [10,13]. Nevertheless, the maximum practical throughput of any configuration is ultimately limited by the flow regimes that emerge during microdroplet formation, as the characteristic squeezing, dripping, and jetting regimes are strongly governed by on-chip hydrodynamics, particularly the continuous phase flow rate and the flow rate ratio between the two phases [14,15]. For high throughput microdroplet generation, flow-focusing devices are commonly operated in the dripping regime at elevated continuous phase flow rates (i.e., at higher capillary numbers), before transitioning into the jetting regime [16]. This operating window not only enables higher microdroplet generation rates, but also maintains a high microdroplet size uniformity, commonly quantified as a Coefficient of Variation (CV). CV, defined as the ratio of the standard deviation of microdroplet diameter to its mean, is expressed as a percentage and serves as a metric for monodispersity. In most published works, a CV below 3% indicates ultra-monodisperse microdroplets, 3%-5% indicates high monodispersity, and 5%-10% moderate monodispersity [17]. CVs exceeding 10% suggest significant polydispersity, which is generally unwanted for applications requiring high precision and reproducibility.

Beyond increasing the throughput of a single mDGU, parallelization is another effective strategy that can be used to increase the total number of generated microdroplets. Parallelized mDGUs integrated into a single platform have been presented in the literature as compact and effective approaches [17], that can be realized by arranging single mDGUs laterally (i.e., side-by-side on one plane, commonly referred to as 2D parallelization), or by stacking them vertically on top of each other (3D parallelization). Lateral parallelization can be realized via all established microfabrication techniques and using a wider range of materials including glass, polydimethylsiloxane (PDMS), or plastics such as polytetrafluorethylen (PTFE), selected based on the intended application. Although effective and methodologically accessible, lateral parallelization is generally limited by footprint, particularly in the case of wafer-based fabrication [18–20]. Furthermore, even when the mDGUs are parallelized laterally, their practical operation often requires vertically stacked layers holding inlets, outlets, flow distribution channels or other operation-related components. One notable lateral parallelization example comes from Yadavali et al., who developed a silicon - glass device that incorporated 10,260 flow-focusing mDGUs on a 4-inch Si wafer, and was able to generate polycaprolactone particles with diameters ranging from 8 to 15 μm (CV<5%) at a rate of 244 g/h, corresponding to 328 billion particles per hour [21]. Another recent example is by Yang et al., who introduced electrostatic field control in an 8-unit PDMS device to produce microdroplets with tunable diameters, demonstrating the potential of active microdroplet generation mechanisms for the parallelization of flow-focusing structures [22].

In contrast to lateral parallelization, vertical parallelization facilitates compact designs, but is more strongly limited by the necessity of precise layer alignment and bonding of multilayer structures. This complicates reproducible platform fabrication and requires additional considerations regarding the mechanical stability of the materials used. These challenges can be addressed using additive manufacturing techniques, which can realize complex geometries without the need of layer alignment and bonding. For example, Femmer et al. utilized digital light processing to fabricate 28 vertically stacked mDGU and generated microgel droplets of 500 μm diameter (CV<5%), reaching a throughput of 3 L/h [23]. Hybrid parallelization techniques have also been demonstrated, in which lateral arrays of mDGUs are also stacked vertically. For example, Kamperman et al. stereolithographically printed three vertical layers of five radially organized flow-focusing mDGU, enabling the generation of microdroplets with a diameter range of 150–1000 μm (CV<10%) [24]. Similarly, Vigogne et al. used projection micro-stereolithography to fabricate 20 laterally parallelized T-junctions in three vertical stacks, a total of 60 units, and implemented downstream microdroplet splitting to produce microdroplets of 169–184 μm diameter [25]. Despite the advantages and demonstrated possibilities, the use of additive manufacturing for the fabrication of microdroplet generating microfluidics is still limited due to material incompatibility with organic solvents, poor surface quality compared to other microfabrication methods and the low resolution of most 3D printing systems that inhibits the fabrication of the microstructures required to produce smaller microdroplets [26]. Utilizing soft lithography, Chung et al. fabricated a multilayer PDMS device containing a total of 1200 high-aspect-ratio rectangular nozzles arranged in three vertical layers of 400 nozzles each. Operating under interfacial tension-driven spontaneous breakup, this platform allowed self-emulsification of highly monodispersed microdroplets of around 45 μm diameter (CV<3%) at frequencies up to 25 kHz [27]. In another example, Conchouso et al. fabricated micromilled and

thermo-compression-bonded multilayer polymethylmethacrylate (PMMA) discs with fractal-like flow distribution networks. This device consisted of four vertical layers, each containing 128 individual flow-focusing units, a total of 512 units, and produced microdroplets with diameters in the range of 150–250 μm (CVs as low as 6%) at a rate of 1 L/h [20]. Similar to the materials used in additive manufacturing, PDMS and PMMA, also suffer from limitations such as solvent incompatibility, low mechanical rigidity, and poor long-term stability.

Given the wide variety of parallelized microdroplet generators reported in literature, differing in terms of microchannel geometry, dimensions, fluid chemistries, device materials, and operating condition, direct performance comparison across studies are inherently difficult, making it difficult to establish quantitative benchmarks. To address this, the present work focuses on a controlled, head-to-head comparison between two parallelization architectures that employ identical droplet generator geometries, but have distinct spatial arrangements. This approach isolates the influence of architectural design on flow behavior and device performance. Specifically, we conduct a systematic comparison between a lateral parallel flow-focusing device (hereafter abbreviated to Lateral-PFFD) and a vertical parallel flow-focusing device (hereafter abbreviated to Vertical-PFFD), to elucidate how geometric configuration governs microdroplet formation dynamics and scalability. Our lateral- and vertical-PFFDs were fabricated out of glass, which combines mechanical robustness, optical transparency, and chemical resistance and enables stable operation across a broad range of flow conditions. Through a combination of flow regime and microdroplet generation mapping, microdroplet size and generation frequency characterization, scaling-law derivation, and inter-channel variability evaluation, we establish understanding and offer design insights related to how geometry affects microdroplet generation stability, throughput, and uniformity in parallelized systems.

2. Materials and methods

2.1. Microfluidic device fabrication

All microfluidic devices were fabricated using 700 μm thick borosilicate glass wafers (Schott, Mainz, Germany). Micropatterning of microchannels, inlets, outlets, and alignment marks were achieved using a ytterbium-doped potassium tungstate (YB:KGW) femtosecond (fs) laser with a wavelength of 1030 nm. The laser was operated at an average power of 8.5 W, a pulse repetition rate of 100 kHz and a scanning speed of 1500 mm/s. Material ablation was performed using a scanning layer consisting of six scanning lines, rotated by 30° to ensure complete 360° coverage, and with a 4 μm spacing between parallel lines. The depth of the patterned microchannels was verified using a Dektak profilometer (Bruker Nano GmbH). Following laser ablation, the patterned wafers were etched for 120 s in a solution containing hydrofluoric acid (HF), phosphoric acid and deionized water to remove debris and minimize surface roughness for improved wettability and stable liquid–liquid interface control within the flow-focusing junction. The wafers were then ultrasonically cleaned in deionized water for 20 min, followed by immersion in piranha solution (sulfuric acid and hydrogen peroxide, 2:1 v/v) for 5 min to enhance surface hydrophilicity. Individual wafers, including the plain borosilicate glass wafer used as a sealing layer, were manually aligned under a microscope via alignment marks to form the respective device structures and were subsequently thermally bonded in a muffle furnace (Laborofen VMK - 135 S Sonder, Linn High Therm GmbH) at 655°C for six hours. A final annealing step was performed at 750°C after bonding in the same muffle furnace for one hour in order to further reduce surface roughness, which was measured using scanning electrode microscopy (SEM, Phenom XL).

2.2. Experimental setup

For microdroplet generation experiments, Lateral-PFFD and Vertical-PFFD were mounted onto a custom two-layer holder consisting of an aluminum upper plate and a Teflon base fixed together using screws to ensure stable positioning during operation. The devices were connected to Teflon tubing (inner diameter 0.5 mm) via NanoPort connectors. The continuous and dispersed phases were delivered to their respective inlets using high-precision syringe pumps (NEMESYS Base 120 equipped with a low-pressure module) fitted with 2.5 mL SETonic microliter syringes. The flow rates of the continuous phase ranged from 5 to 270 μL/ min, while those of the dispersed phase varied between 3 and 100 μL/min, depending on the experimental conditions (see **Section 3**). All reported flow rates refer to the total inlet flow to the system. All microfluidic experiments were conducted in a temperature-controlled laboratory at 22 ± 0.5 °C.

2.3. Materials

In all experiments, the continuous phase was an aqueous solution: 50 mM Tris buffer, prepared from Tris base (Fisher Bioreagents, Germany, product number 10103203, molecular biology grade) and adjusted to pH 7.0, containing 1% Tween 20 (Sigma Aldrich, Germany, product number P1379) as a surfactant. The dispersed phase was methyl tert-butyl ether (MTBE, Honeywell, Germany, product number 20256, ≥99.8% purity, residue analysis grade), an organic compound commonly used in research laboratories. All chemicals were analytical-grade reagents obtained from commercial suppliers and were used as received without further purification.

2.4. Measurement of fluid density, viscosity and interfacial tension

The densities of the continuous and dispersed phases were measured at 22 °C using a vibrating-tube densimeter (DMA 35, Anton Paar, Austria). The measured density of the buffer solution was 1.003 g cm^{-3} , while that of methyl tert-butyl ether (MTBE) was 0.741 g cm^{-3} .

Dynamic viscosity was measured with a rotational rheometer (Anton Paar Physica MCR 101) at 22 °C under a controlled shear-rate sweep from 1 to 1000 s^{-1} . Temperature was held within ±0.1 °C by the instrument's Peltier unit. Three independent sweeps were recorded for each liquid. To avoid start-up artifacts and physically implausible readings, we excluded the first point when it showed transient behaviour and applied pre-specified plausibility windows: 0.9–1.2 mPa·s for the aqueous buffer and 0–0.5 mPa·s for MTBE. All remaining points were pooled across replicates. The buffer behaved as a Newtonian fluid over the tested range (variation < 2%), yielding a dynamic viscosity of 1.064 ± 0.013 mPa·s (n = 55). MTBE also showed a shear-independent viscosity within experimental uncertainty of 0.293 ± 0.016 mPa·s (n = 54). Reported values are mean ± SD of all accepted data points.

The interfacial tension between MTBE and the buffer phase was measured using the pendant-drop method on a Krüss DSA 100E at 22 °C. In each run, a droplet of MTBE was formed at the tip of a stainless-steel needle submerged in buffer and was monitored for 1 min while images were recorded every 5 s to capture the equilibrium profile. The procedure was repeated three times under identical conditions. All measurements were processed using the ADVANCE software, which fitted the droplet shape to the Young–Laplace equation to determine the interfacial tension. The resulting static interfacial tension was 3.22 ± 0.05 mN m^{-1} .

2.5. Microfluidic droplet imaging and detection

The complete methodology for microfluidic droplet detection has been described in a previous work, where microfluidic droplets were systematically investigated as vessels for two-phase biocatalysis [28]. Briefly, 3D digital microscopy (Keyence VHX-5000) was used to observe microdroplet formation, verify stable operation throughout the experiments, and capture microdroplet images. To evaluate microdroplet characteristics, such as size and shape, microdroplets within one field of

view (FOV) of 400 μm x 2602 μm were detected using a neural network trained to denoise and segment the original images. In this pipeline, microscopy images of microdroplets were first pre-processed by manually segmenting inverted 16-bit grayscale images (~180 ×1200 pixels) to section microdroplets formed across a range of continuous-to-dispersed phase flow rate ratios. After preprocessing, microdroplet boundaries were identified and outlined using the Hough Circle Transform (HCT) with optimized parameters, including a radius search increment of 1 and a maximum circle score of 1200. Finally, circular masks were superimposed on the denoised images to verify detection efficiency. All droplet measurements were performed at a fixed downstream observation position, approximately 5 mm away from the nozzle, ensuring consistent sampling conditions across experiments. The reliability of the droplet detection pipeline was evaluated using 15 representative microscopy images containing 3148 droplets in total. Automated detection results were compared with manual annotations, yielding a precision of 96.8%, recall of 97.7%, and an F1 score of 97.2%.

3. Results and discussion

3.1. Microfluidic device design

We fabricated and evaluated two microfluidic devices: a Lateral-PFFD and a Vertical-PFFD, each integrating three mDGUs, allowing direct performance comparison under identical operating conditions. Each mDGU operates based on a flow-focusing configuration, in which the continuous phase, introduced through two side channels, pinches the dispersed phase entering from a central inlet, resulting in microdroplet formation at a narrow constriction (Figure S1). All individual mDGUs were designed to have a main channel length of 22 mm, a depth of 100 μm, and a width of 400 μm. The geometry of the flow-focusing region was optimized to ensure stable and reproducible microdroplet breakup over a broad range of flow conditions. Related device design details can be found in Supporting Information (SI).

In the Lateral-PFFD, the three units were arranged side by side in one planar layer, sharing all inlets and the outlet (Fig. 1**a**). Microfluidic channels were structured into the top glass wafer. Shared inlet and outlet distribution channels for the continuous and dispersed phases were structured into the bottom glass wafer. The middle wafer served as a spacer and contained vertically aligned through-holes connecting the top and bottom wafers. To ensure equivalent flow distribution among the three mDGUs, the inlet and outlet channels were designed to have equal hydraulic resistances. Based on the Hagen–Poiseuille principle for laminar flow [29], the hydraulic resistance R, in rectangular microchannels is given by $R = \frac{12\mu L}{wh^3(1-0.630\frac{h}{w})}$, where μ is the dynamic viscosity of the flowing phase, w is the width, h is the height, and L is the length of the channel. Accordingly, the hydraulic resistance of the three individual continuous phase inlets was 4.1×10^{11} Pa·s·m^{-3} and that of the three individual dispersed phase inlets was 1.2×10^{11} Pa·s·m^{-3}. Similarly, the hydraulic resistance of the individual outlet channels was 8.4×10^{11} Pa·s·m^{-3}.

The Vertical-PFFD consists of three stacked mDGUs, each structured into a separate glass wafer (Fig. 1**b**), significantly reducing device footprint. To enable simultaneous optical imaging of all layers, the channel positions were slightly offset laterally. The stack was sealed with an additional blank glass wafer (top layer). As in the Lateral-PFFD device, the three mDGUs share a continuous phase inlet, a dispersed phase inlet and an outlet for microdroplet collection. To ensure negligible inlet fluidic resistance and equal flow distribution into the three mDGUs, the cylindrical inlet (feed) channels (750 μm bottom diameter, 2.1 mm height) were designed according to the design criterion 2 N(Rr/Rd) < 0.01 [30], where Rr is the fluidic resistance along the delivery channel between adjacent mDGU, Rd is the fluidic resistance of individual mDGUs, and N is the number of mDGUs. This criterion ensures that the pressure drop along the feed channel remains insignificant compared to that across each generator, leading to uniform flow distribution among all layers and preventing preferential flow into specific mDGUs.

To verify that the proposed device geometries ensure equivalent flow distribution among the three mDUGs, computational fluid dynamics (CFD) simulations were performed using COMSOL Multiphysics to investigate the pressure fields in the two architectures. As shown in Figure S2, in the Lateral-PFFD configuration each branch consists of a wider feed channel followed by a narrower channel representing the equivalent hydraulic resistance of the mDGU. This architecture can therefore be interpreted as a hydraulic equivalent circuit in which the feed channel and the mDGU resistance are connected in series. In the Vertical-PFFD configuration, a wider feed channel supplies all three downstream channels, which can be interpreted as a hydraulic equivalent circuit consisting of a common feed channel connected to three mDGU resistances arranged in parallel. These CFD results confirm the identical pressure distributions in the three mDGUs for both architectures, as per our design presented above.

3.2. Baseline conditions for parallel device comparison

Microdroplet formation in flow-focusing microfluidic devices is governed by several key parameters, including fluid properties (such as viscosity, interfacial tension, and density), the geometry of the device (particularly the size and shape of the orifice and channels), as well as the flow rates of the continuous and dispersed phases, where the flow rate directly affects microdroplet size and generation frequency. To ensure a rigorous and unbiased comparison between the Vertical- and Lateral-PFFD architectures, all baseline experimental conditions, such as the geometry (discussed in **Section 3.1** above), fluid composition, operational procedures, and device handling were carefully controlled

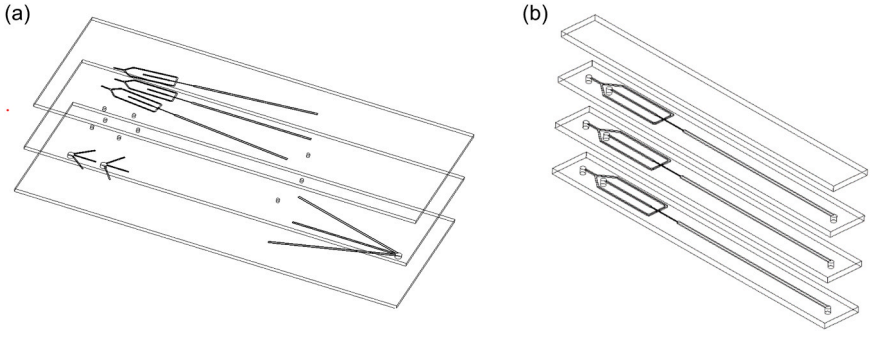

Fig. 1. Exploded view of parallelized multilayer microfluidic devices. (a) The Lateral-PFFD consists of three mDGUs arranged laterally in a single layer. The inlet and outlet channels were designed with equivalent hydraulic resistances to ensure equal flow distribution between mDGUs. (b) The Vertical-PFFD features a stacked configuration, where each mDGU is fabricated in a separate layer. In both configurations, the mDGUs share inlets for the continuous and dispersed phases, as well as a single outlet for microdroplet collection.

and matched across devices. To explore the scalability of monodisperse microdroplet generation at high throughput, parameters such as continuous and dispersed phase flow rates, flow rate ratios and fluid viscosity were systematically varied to investigate their influence on microdroplet formation. At every experimental point, the same conditions were applied to both devices enabling direct performance comparison in terms of microdroplet diameter, CV, generation frequency and operational stability. To exclude confounding effects from fabrication variability, we first confirmed channel geometry for both architectures and found that channel depth and width were highly uniform within each mDGU and consistent between mDGUs, demonstrating excellent dimensional stability (Figure S3, Table S1–S3). By verifying geometric consistency, and in combination with identical operational conditions, we can attribute any differences observed between parallelized devices solely to the architecture. In addition, surface roughness of the microchannels was characterized to minimize potential effects arising from wall irregularities and to ensure comparably smooth channel surfaces for both device architectures. The corresponding surface roughness measurements are provided in Figure S4. The optimized surface roughness (Sq=209 ± 8.50 nm) is several orders of magnitude smaller than the characteristic channel dimension, and therefore its influence on droplet breakup is expected to be negligible.

3.3. Flow regime and microdroplet generation regime mapping

As the flow rates of the continuous phase (Q_c) and dispersed phase (Q_d), and in particular their ratio, can have a significant impact on the flow regime established in flow focusing devices, we systematically varied these rates and mapped the resulting hydrodynamic regimes in Fig. 2; squeezing (pink), dripping (blue), jetting (green), transition from squeezing to dripping (orange) and transition from dripping to jetting (yellow).

Supplementary material related to this article can be found online at doi:10.1016/j.colsurfa.2026.140587.

Supplementary material related to this article can be found online at doi:10.1016/j.colsurfa.2026.140587.

Supplementary material related to this article can be found online at doi:10.1016/j.colsurfa.2026.140587.

Overall, both PFFD exhibited similar trends. At low to high Q_c and low Q_d, flow was characterized by dripping as viscous forces and capillary forces of comparable magnitude allowed shear stress and interfacial tension to reach a dynamic balance in which the continuous phase periodically pinched off the dispersed thread at the orifice. As Q_d increased, jetting emerged for intermediate to high Q_c, as the shear and viscous stresses dominated over surface tension, stretching the dispersed phase into a continuous liquid jet that broke irregularly downstream. Squeezing was limited to low Q_c across most Q_d, when the shear stress exerted by the continuous phase is insufficient to overcome the viscous resistance and interfacial tension of the dispersed phase, resulting in the dispersed phase being slowly extruded from the orifice. Transitional regimes appeared between established flow regimes.

Despite the similarities in the general flow regime trends, the two device configurations also exhibited distinct differences. For example, in the Lateral-PFFD, no microdroplet formation occurred when both Q_c and Q_d were very low (≤10 μL/min, white block on Fig. 2**a**). This is due to viscous displacement as the pressure drop along the distribution channels upstream of the mDGUs was comparable to the inlet driving pressure, preventing the dispersed phase from entering the junction. Conversely, the Vertical-PFFD required no flow distribution channels, ensuring stable two-phase convergence even at low inlet flow rates. Additionally, the Lateral-PFFD exhibited a slightly wider dripping window, which can be attributed to the lateral geometry providing additional flow damping at moderate flow rates, thus reducing instantaneous shear fluctuations. On the other hand, the Vertical-PFFD exhibited a broader jetting region that can be explained by the vertical supply layout providing more uniform pressure distribution at high flow rates, focusing shear stress at the junction and enabling stable operation at higher throughputs. Representative videos of all flow regimes are provided in **Videos S1–5**.

For completeness, we also replotted the regime map using the capillary number of the continuous phase (on the x-axis) and the capillary number of the dispersed phase (on the y-axis) as defined by $Ca_c = \mu_c U_c/\gamma$ and $Ca_d = \mu_d U_d/\gamma$ respectively. Both capillary numbers are defined locally at the droplet-generation junction based on the nominal single-channel velocities. μ_c and μ_d are the viscosities of the continuous and dispersed phase, U_c and U_d the velocities of the continuous and dispersed phase and γ is the interfacial tension between two phases (Figure S5). Since the same continuous and dispersed phases were used

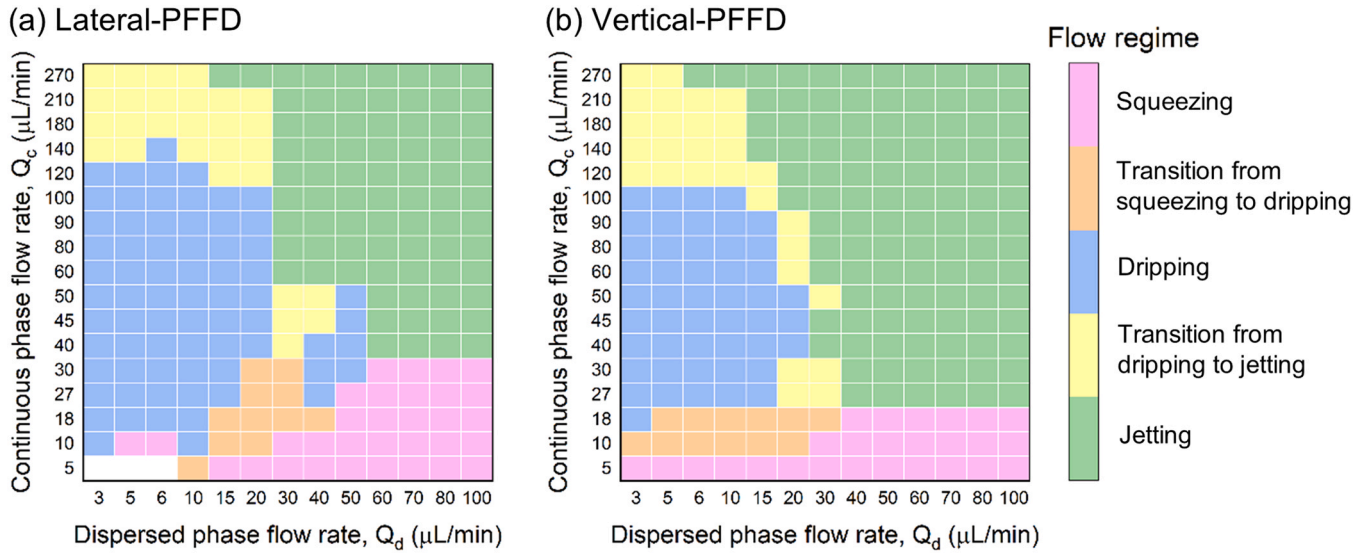

Fig. 2. Microdroplet generation flow regime map of PFFD at varying Q_c and Q_d (in μL/min). Each cell on this map represents one flow rate ratio. (a) Lateral-PFFD. At very low Q_c and Q_d, no microdroplet formation occurs due to viscous displacement in the upstream channel (white region). (b) Vertical-PFFD. Compared with the Lateral-PFFD, the Vertical-PFFD exhibits a broader jetting region extending toward lower Q_c and Q_d, while the dripping regime remains confined to a narrower band at intermediate Q_c and low Q_d. Finally, the squeezing regime was confined at low Q_c for all Q_d. All experiments were repeated at least three times, and all three parallel channels showed identical flow regimes at given flow rate ratios. Representative videos of these flow regimes are provided in **Videos S1-5**.

for all experiments, the capillary numbers are directly proportional to the corresponding flow rates, leading to equivalent regime boundaries to the ones presented in Fig. 2.

To connect the flow regimes identified in Fig. 2 with their practical outcomes, we mapped the corresponding microdroplet geometries produced at the same flow rate combinations. For this analysis, microdroplet images were recorded downstream of the flow focusing junction in the main channel. Fig. 3 presents the microdroplet state maps. As above, each cell represents a unique pair of Q_c and Q_d, and the colors indicate the observed microdroplet states: green for monodisperse microdroplets (CV<10%), yellow for polydisperse microdroplets (CV≥10%), orange for mixed flow of microdroplets and slugs, and pink for slug flow. Representative microscopy images of each state are shown in the color bar.

When compared with the flow regime maps in Fig. 2, it becomes evident that the flow regime and microdroplet generation regime are not in one-to-one correspondence. In these devices, microdroplets with CV< 10% were generated not only in the dripping regime characterized by periodic pinch-off process at the junction, but also across most of the jetting regime, particularly at high Q_c and Q_d where the increased flow momentum stabilizes the jet and promotes periodic breakup. These observations indicate that microdroplet monodispersity cannot be directly inferred from the hydrodynamic mode alone. A quantitative comparison of the microdroplet generation regime maps shows that approximately 67% of the operating conditions tested led to the generation of monodisperse microdroplets (green region) in the Lateral-PFFD, compared to 62% in the Vertical-PFFD. The slightly larger monodisperse operating window in the Lateral-PFFD can be attributed to more uniform shear and a more stable breakup process, as flow focusing and downstream transport occur within a single plane, compared to the 3D flow transitions and vertical offsets in the Vertical-PFFD that can slightly perturb the jet. In the transitional flow regimes, the breakup behavior becomes less stable, which leads to the formation of polydisperse microdroplets, though monodisperse microdroplets may still form when a stable periodic cycle is maintained. As dripping transitions to squeezing, the dispersed phase occupies most of the channel cross-section, resulting in elongated slug microdroplets. Overall, these results indicate that microdroplet monodispersity is not directly dictated by the flow regime, but also depends on the flow rates and their ratio, which together determine the shear strength and breakup frequency at the flow focusing junction. As above, the microdroplet state map replotted using the capillary numbers of the continuous and dispersed phases is also presented in Figure S6.

3.4. Microdroplet generation characteristics

To compare the performance of the Lateral- and Vertical-PFFD in terms of throughput, we systematically varied the continuous-to-dispersed phase flow rate ratio (defined hereafter as Φ=Qc/Qd) and recorded the microdroplet generation frequency (Fig. 4). Our analysis focused primarily on the green region on the color maps of Fig. 3, as it corresponds to the flow conditions that allow stable and monodisperse microdroplet generation. Four continuous-to-dispersed phase flow rate ratios were selected for testing: 1:2 (Φ=0.5), 1:1 (Φ=1), 3:1 (Φ=3), and 9:1 (Φ=9). Flow rate ratios with a lower continuous phase fraction, such as 0.33 or 0.25, could not produce stable microdroplet flow (see example flow rates of 10:30 μL/min or 10:40 μl/min in color maps above) and were therefore excluded. For Φ = 0.5, only two flow rate combinations are included because the operating window that yields microdroplets with CV < 10% is narrow, indicated in green in the microdroplet generation regime map in Fig. 3. The analytical expression used to calculate the microdroplet generation frequency is presented in Equation S1 and a detailed derivation is provided in SI.

As observed in Fig. 4, for both the Lateral-PFFD and Vertical-PFFD, increasing the total flow rate at any fixed flow rate ratio results in higher microdroplet generation frequency. The two devices generate microdroplets at comparable frequencies at most flow rates and flow rate ratios, with the Vertical-PFFD consistently, but marginally, outperforming the Lateral-PFFD. However, at very high flow rates and high Φ the throughput of these devices diverges in a noticeable way. Specifically, at 270:30 μL/min (Φ=9) the Vertical-PFFD reaches a microdroplet generation frequency of up to 33 kHz, which is comparable to some of the highest microdroplet generation frequencies reported in previous studies on parallelized microdroplet generation [27]. At the same flow rates, the Lateral-PFFD only reaches a frequency of 22 kHz, a difference of 11k generated microdroplets per second. Similarly, at 180:60 μL/min (Φ=3), the Vertical-PFFD outperforms the Lateral-PFFD by around 4.8k generated microdroplets per second. The lower microdroplet generation frequency observed in the Lateral-PFFD at high flow rates can again be attributed to slightly slower build-up of shear, and consequently lower microdroplet pinch-off rate at the orifice, a consequence of the longer flow paths through the feed channels. At the same

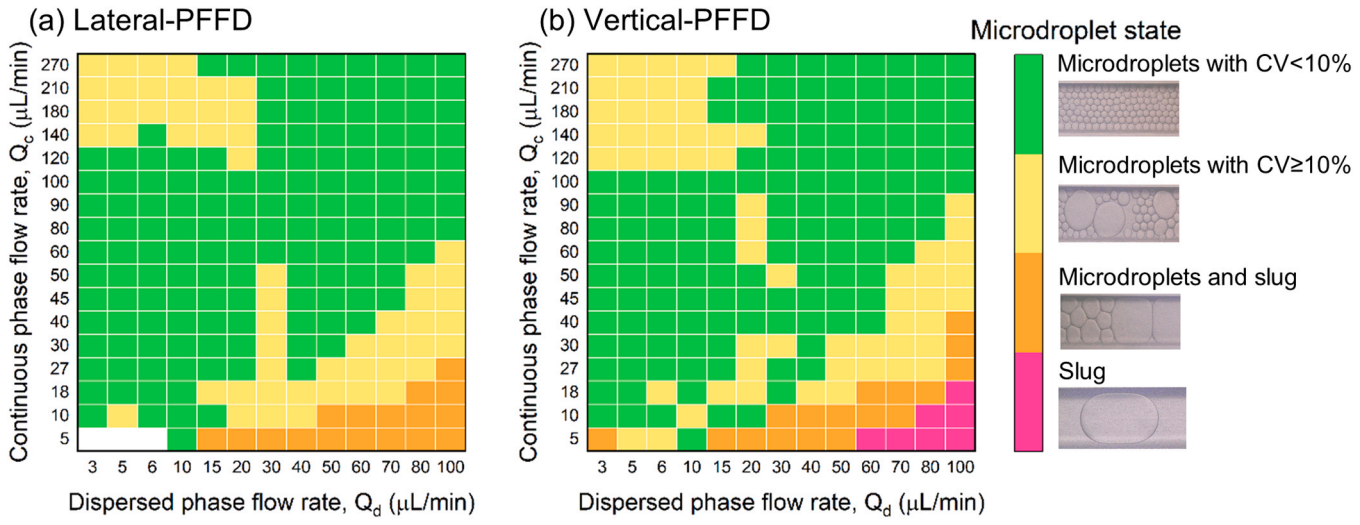

Fig. 3. Microdroplet generation regime map of (a) Lateral-PFFD and (b) Vertical-PFFD at varying continuous phase and dispersed phase flow rate combinations (μL/min). Each cell represents one unique pair of Qc and Qd. The colors denote different microdroplet generation states: green for monodisperse microdroplets (CV<10%), yellow for polydisperse microdroplets (CV≥10%), orange for coexistence of microdroplets and slug segments, and pink for slug flow. Representative optical micrographs of each state are shown as part of the color bar.

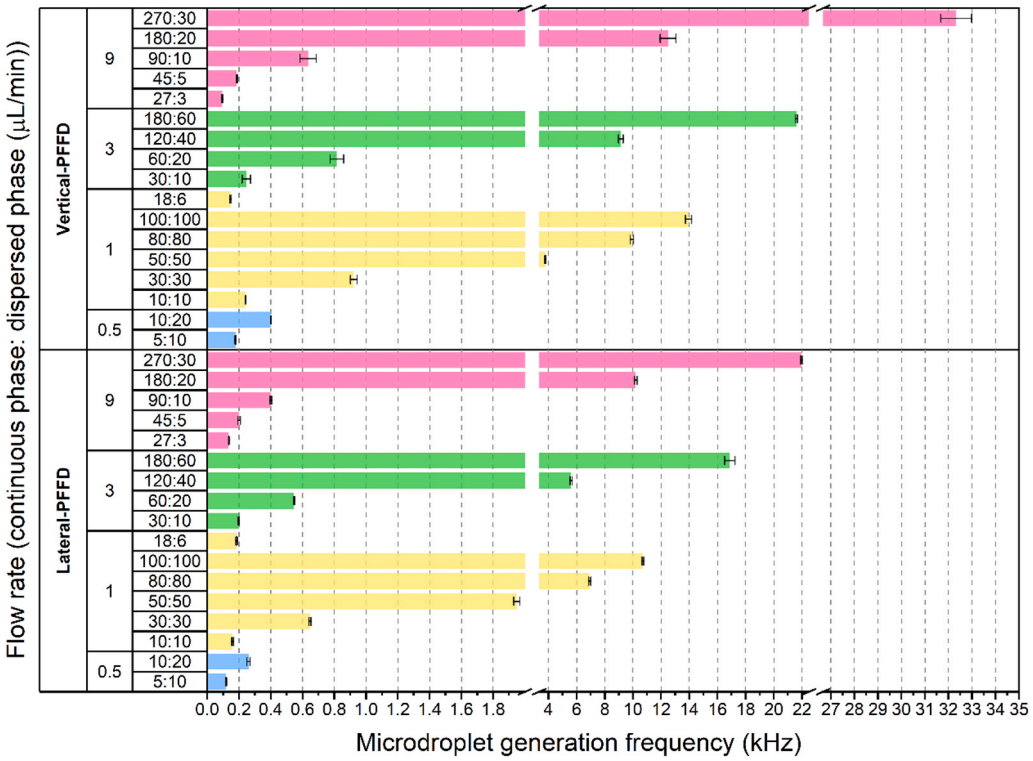

Fig. 4. Microdroplet generation frequency in Lateral- and Vertical-PFFD at Φ= 0.5, 1, 3 and 9. For each Φ, multiple flow rate combinations (in μL/min) were tested (shown in the third column). Microdroplet generation frequency was extracted from the total number of microdroplets (generated in all three channels) observed in a single field of view (size: 400 μm × 2602 μm, one FOV for each channel) at the corresponding flow rate. Error bars represent the standard deviation from at least three technical replicates. The Vertical-PFFD consistently achieved higher microdroplet generation frequencies, especially at very high flow rates, highlighting its superior throughput performance.

flow rate ratios (Φ=9 and 3), no significant difference was observed between the microdroplet generation frequencies in the two device configurations at lower flow rates. These results highlight, in a quantifiable way, the throughput advantage of the Vertical-PFFD configuration at high flow rates.

In addition to microdroplet generation frequency, microdroplet size and monodispersity (in terms of CV) were evaluated for the same Φ and flow rates as in Fig. 4. The results are visualized in Fig. 5. As in Fig. 4, for $\Phi = 0.5$, only two flow rate combinations are included because the operating window that yields microdroplets with CV $< 10\%$ is very narrow. In terms of microdroplet diameter, both devices exhibited a similar overall trend: as the total flow rate increased, the average microdroplet diameter decreased. However, the Vertical-PFFD produced smaller microdroplets than the Lateral-PFFD (blue line plot vs pink line plot) at all flow rates, consistent with overall stronger local shear at the junction. The smallest microdroplets produced by the Vertical-PFFD had a diameter of 21.9 ± 1.49 μm, while the smallest microdroplets produced by the Lateral-PFFD had a diameter of 29.2 ± 1.02 μm (both at 270:30 μL/min continuous-to-dispersed phase flow rate). Microdroplet CV is presented in the bar plots of Fig. 5 and a vertical red line is added to indicate CV= 10% for better result visualization. As the tested flow rates covered all observed flow regimes visualized in the color map of Fig. 2 and not only the dripping regime, their CV of droplet size did not vary monotonically with flow conditions. Similarly, the flow rate combination where CV exceeded 10% (10:20, 30:30, and 180:20 μL/min for the Lateral-PFFD, and 10:10, 30:30, 18:6, and 60:20 μL/min for the Vertical-PFFD), were found to correspond to the transitional regions, where microdroplet pinch-off becomes unstable and size distribution broadens. In contrast, for all flow rates that fall clearly within either the dripping or jetting regime, CV remained below 10% in both device configurations, indicating that variations in microdroplet monodispersity arise from the intrinsic instability of the transitional regimes rather than device geometry. Notably, both devices achieved highly monodisperse microdroplet generation under stable dripping conditions, namely, CV of 1.7% at 45:5 μL/min (shaded pink bar in (d)) in the Vertical-PFFD closely followed by CV of 2.3% at 90:10 μL/min (shaded blue bar in (d)) in the Lateral-PFFD, demonstrating that both configurations can produce microdroplets with uniformity sufficient for the vast majority of microdroplet-based microfluidic applications, including encapsulation, emulsions, assays, and material synthesis. However, the same is not true for the monodispersity reached at the highest flow rates investigated. At 270:30 μL/min, the Lateral-PFFD maintained high monodispersity with a CV of 3.5%, as opposed to a CV of 6.8% in the Vertical-PFFD. This establishes a trade-off between throughput (highest for the Vertical-PFFD at these flow rates, see Fig. 4) and monodispersity, which should be considered according to the desired application, as a CV close to 7% is considered too high for high-precision applications such as single-cell or single-molecule assays or nanomaterial templating.

3.5. *Scaling analysis of microdroplet formation*

To quantitatively interpret the experimental trends observed in the previous section, we performed a scaling analysis to establish explicit physical relationships governing microdroplet formation in both PFFDs. While the experiments presented in the sections above provide a clear qualitative picture, for example, showing how microdroplet frequency (in Fig. 4) and size (in Fig. 5) vary with operating conditions and parallelization architectures, they do not quantify the relative importance of the underlying parameters. Here, we derive compact scaling relations that disentangle the contributions of volumetric throughput and capillary effects, and quantify how the two architectures modulate these dependencies for microdroplet generation frequency and, subsequently, microdroplet size. As a baseline for our scaling analysis, we constrain microdroplet generation frequency in flow focusing devices by volume

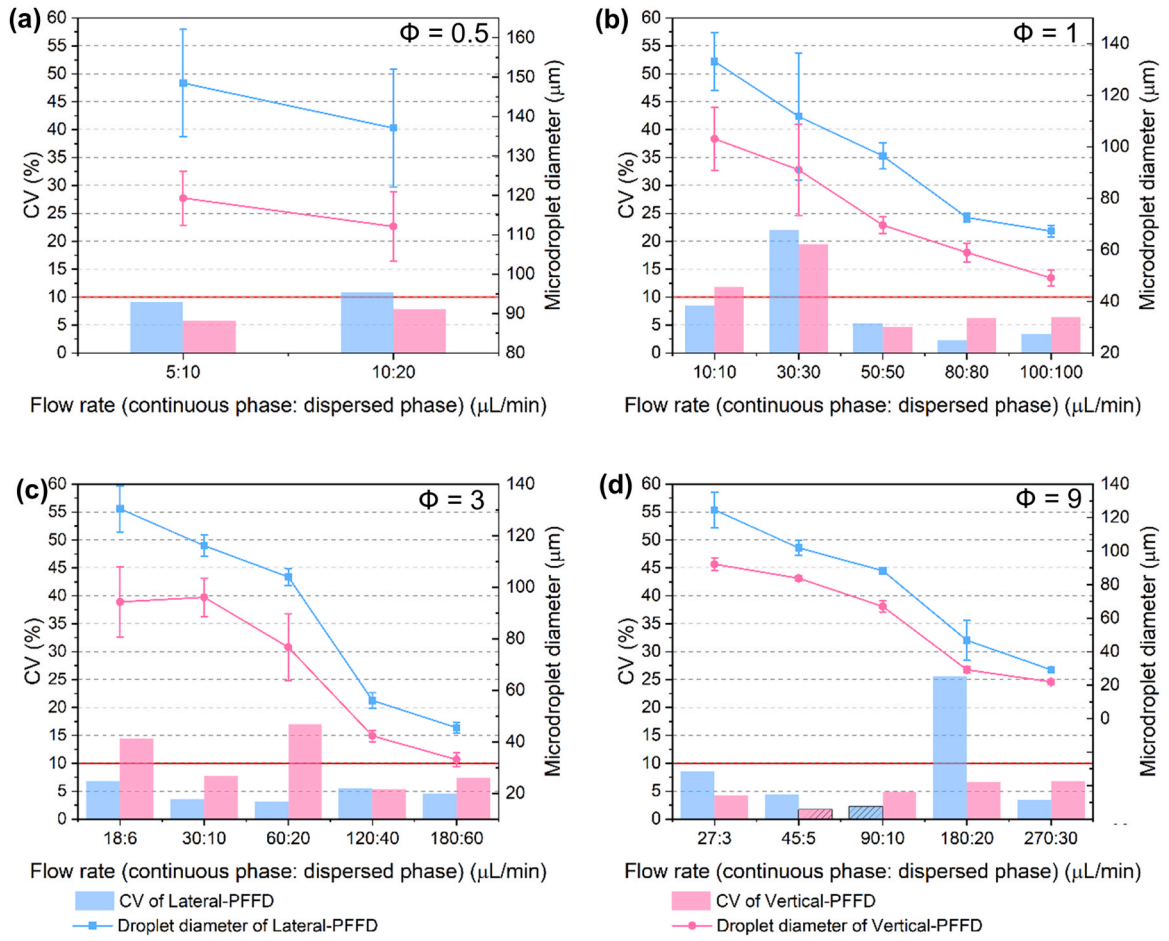

Fig. 5. Comparison of microdroplet diameter (right y-axis) and monodispersity (in CV, left y-axis) in Lateral- and Vertical-PFFD at: (a) Φ= 0.5, (b) Φ= 1, (c) Φ= 3, and (d) Φ= 9. For each ratio, multiple flow rates were tested. The red vertical lines indicate CV= 10%. Error bars represent the standard deviation from at least three technical replicates. The Vertical-PFFD produces smaller microdroplets at all flow rates. The smallest microdroplets had a diameter of 22 μm and were produced at 270:30 continuous-to-dispersed phase flow rate ratio. Monodispersity fluctuates with flow rate, and is only found to exceed 10% at flow conditions corresponding to the transition between flow regimes explained by increased instability during microdroplet pinch-off. The lowest CV of 1.7% was achieved by the Vertical-PFFD at 45:5 μL/min (shaded pink bar in (d)) closely followed by CV of 2.26% at 90:10 μL/min (shaded blue bar in (d)) in the Lateral-PFFD. In figure (d), the right y-axis was offset to facilitate visualization in this dual-y-axis chart.

conservation. The injected dispersed phase is partitioned into a sequence of microdroplets that detach at a characteristic frequency once interfacial stresses overcome confinement and viscous forces. This simple scaling was verified for both PFFDs and is summarized in Equation S2 and Figure S7. For the fitting, we used experimentally measured microdroplet generation frequencies and diameters obtained under operating conditions that produced monodisperse microdroplets (CV<10%). Deviations from the volume-conservation scaling reflect non-ideal microdroplet dynamics, such as transient storage of the dispersed phase, satellite microdroplet formation, or departures from sphericity, which are commonly analysed in the squeezing, dripping and jetting regimes of flow-focusing generators [31,32]. Under such conditions, volume conservation alone is insufficient to distinguish whether microdroplet breakup is primarily governed by flow rate partitioning or by interfacial stresses. We therefore introduce a refined power-law scaling that explicitly incorporates Φ defined as Q_c/Q_d and the capillary number of the continuous phase. For each individual channel:

$$f(Hz) = A\,\Phi^{\alpha} Ca_c^{\beta} \left(\frac{Q_d}{d^3}\right)^{n}, \tag{1}$$

where A is an effective prefactor that captures non-ideal effects, and the fitted scaling exponents α and β quantify how strongly the microdroplet generation frequency responds to variations in Φ and the channel capillary number (Ca_c), respectively. The refined power law was refitted to the same empirical data as in Figure S7 for the two device configurations using multivariate linear regression in logarithmic (log–log) space. For the Lateral-PFFD the best fit was: $f = 3.99\left(\frac{Q_d}{d^3}\right)^{0.87}\Phi^{-0.03}Ca_c^{-0.05}$ ($R^2 = 0.982$), with both scaling exponents α and β being near zero (−0.03 and −0.05 respectively) indicating that within the investigated range the microdroplet generation frequency is only weakly sensitive to variations in flow rate ratio (Φ reduces f by 8.3%) and capillary number (Ca_c reduces f by 15.2%), and is primarily governed by the volumetric term (327-fold increase over the explored $\frac{Q_d}{d^3}$ range). From a physical perspective, this weak dependence can be attributed to the fact that, within the stable monodisperse droplet generation regime explored in this study, droplet formation is primarily governed by volumetric throughput rather than interfacial dynamics. The dominant term Qd/d_3 reflects the volumetric constraint linking dispersed phase flow rate to droplet size and generation frequency, whereas Φ and Ca_c mainly influence local deformation and pinch-off dynamics, resulting in only secondary corrections to the overall frequency. In contrast, for the Vertical-PFFD fitting yielded $f = 9.97\left(\frac{Q_d}{d^3}\right)^{0.84}\Phi^{-0.22}Ca_c^{0.18}$ ($R^2 = 0.998$), indicating a moderate effect of Φ and Ca_c on microdroplet generation frequency. Over the investigated Φ range, frequency was reduced by 47.1%, while variations in Ca_c increase it by up to a factor of 2; nevertheless, the volumetric term

remains dominant (259-fold increase over the explored $\frac{Q_d}{d^5}$ range). According to the fitting, increasing Φ leads to a reduction in microdroplet generation frequency (evidenced by the negative exponent), consistent with enhanced stretching and transient storage of the dispersed thread. Increasing Ca_c promotes higher frequencies through stronger viscous squeezing at the junction. This enhanced sensitivity arises from the more direct and efficient pressure transmission in the vertical geometry, which allows local shear and interfacial deformation to respond more immediately to changes in operating conditions. Although secondary to the still dominant volumetric scaling, these effects represent meaningful corrections that capture how non-ideal hydrodynamics, and by extension device architecture, influence microdroplet breakup.

CFD simulations of the pressure fields (Figure S2) further support this interpretation from a hydrodynamic perspective. As discussed in **Section 3.1**, the simulations reveal that in the Lateral-PFFD architecture the pressure drops progressively along the individual feed channels before reaching the equivalent mDGU hydraulic resistances. In contrast, the Vertical-PFFD configuration results in more direct pressure transmission to the downstream mDUGs. This difference in pressure transmission pathways is consistent with the experimental observation that the Vertical-PFFD exhibits higher droplet generation frequencies and a stronger sensitivity to operating conditions, and provides additional hydrodynamic support for the refined scaling relationships and the architecture effects discussed above.

In addition to microdroplet generation frequency, microdroplet size also follows a similar characteristic scaling relationship, widely reported in previous studies of microfluidic flow-focusing systems [33]. The normalized microdroplet diameter can be correlated with Ca_c and Φ through the following power-law:

$$\frac{d}{w} = KCa_c^{\gamma}\,\Phi^{\delta}, \tag{2}$$

where d is microdroplet diameter, w is the characteristic junction width (which equals 50 μm in both devices) and K, γ and δ are empirical constants determined from fitting. For the Lateral- and Vertical-PFFD, fitting yielded the following relationships, respectively: $\frac{d}{W} = 0.274\ Ca_c^{-0.457}\ \Phi^{0.03} (R^2 = 0.846)$ and $\frac{d}{W} = 0.202 Ca_c^{-0.448}\ \Phi^{0.049}\ (R^2 = 0.847)$, visualized in Fig. 6. The fitted planes (blue for the Lateral-PFFD and pink for the Vertical-PFFD) clearly illustrate that both geometries follow the same qualitative trend: microdroplet size decreases with increasing Ca_c and decreasing Φ. However, the fitted plane for the Lateral-PFFD lies systematically above that of the Vertical-PFFD, indicating that under comparable operating conditions, the lateral geometry yields larger microdroplets. This difference is also reflected in the fitted prefactors K (0.274 and 0.202 for the Lateral-PFFD and Vertical-PFFD respectively) and it shows the same trend as Fig. 4, which suggests that the vertical geometry provides more efficient hydrodynamic focusing and pinch-off, consistent with stronger confinement and direct pressure transmission.

In terms of fitting outcomes, both device geometries exhibit a negative correlation between d/w and Ca_c, consistent with the enhanced shear imposed by the continuous phase. This trend can also be observed in Fig. 5. For example, in the Lateral-PFFD at a fixed Φ= 3, increasing the continuous phase flow rate from 18 μL/min to 180 μL/min (i.e., increasing Ca_c) reduces the microdroplet diameter from 130.4 μm to 45.5 μm. The corresponding dependence on Φ is considerably weaker as reflected by the small exponents (0.03 for Lateral-PFFD and 0.049 for Vertical-PFFD), indicating robust microdroplet diameter that is insensitive to relative flow rates between continuous and dispersed phases. As with Ca_c, this weak correlation between Φ and microdroplet diameter can also be observed in Fig. 5. For example, when the continuous phase flow rate is held constant at 180 μL/min (keeping Ca_c constant) and Φ is increased from 3 to 9, the microdroplet diameter in the Vertical-PFFD changes only from around 29 μm to 32 μm.

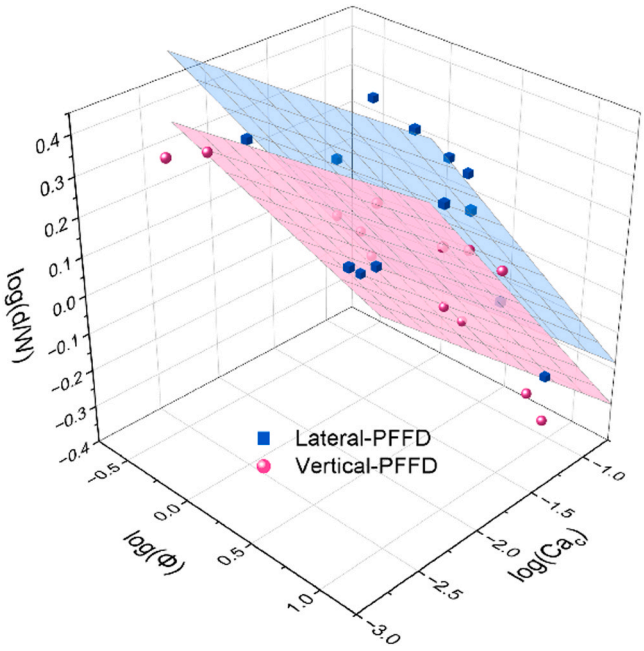

Fig. 6. Graphical visualization of normalized microdroplet diameter (d/W, W=50 μm is the width of the nozzle) dependence on Ca_c and Φ. Devices were compared under identical conditions. The fitted planes represent power-law regressions (blue for Lateral-PFFD and pink for Vertical-PFFD). The fittings yield the following correlations: Lateral-PFFD: $\frac{d}{W} = 0.274 Ca_c^{-0.457}\ \Phi^{0.03}, R^2 = 0.846$ and Vertical-PFFD: $\frac{d}{W} = 0.202 Ca_c^{-0.448} \Phi^{0.049}, R^2 = 0.847$. All three axes are plotted in logarithmic scale to visualize the linearity of the relationship. In both devices microdroplet size decreases with increasing Ca_c and decreasing Φ, however, the fitted plane for the Lateral-PFFD lies systematically above that of the Vertical-PFFD, indicating that under comparable operating conditions, the lateral geometry yields larger microdroplets. The regression quality is comparable for both devices ($R^2 \approx 0.85$), suggesting that the power law model has a strong relationship with the data capturing most of the variability. The residual scatter could be attributable to wetting dynamics, satellite microdroplet formation, and parallelization-induced flow imbalances.

To make the empirical scaling relationships developed here directly usable, we developed an interactive web application based on the R/Shiny platform that allows users to estimate operating conditions for the PFFD devices [34]. Users select the device (Lateral-PFFD or Vertical-PFFD) and input relevant physical parameters, including the continuous phase viscosity, interfacial tension, flow rate ratio, and the target microdroplet generation frequency. The app then calculates the corresponding operational point, specifically, the dispersed phase flow rate, continuous phase flow rate and an estimated microdroplet diameter, based on the empirical scaling laws derived from our experimental data, with microdroplet diameter and generation frequency evaluated using Eqs. 2 and 1, respectively. For a specified target frequency, a one-dimensional root-finding procedure is implemented to solve for the continuous-phase flow rate and the corresponding dispersed-phase flow rate. The predicted operating point is subsequently visualised on the experimental regime map by snapping to the nearest grid cell, and an extrapolation indicator is provided to flag conditions outside the experimentally sampled parameter ranges. While the predictions are specific to the devices studied here, this tool provides a practical guide for exploring operational windows based on the empirical scaling relationships derived from the present experimental dataset, planning experiments, and understanding how variations in physical and flow parameters influence microdroplet formation. While the model captures the dominant trends observed experimentally, deviations between predicted and measured operating conditions may arise from the inverse nature of the scaling relationships and the non-uniqueness of flow-rate

combinations that yield similar droplet generation frequencies.

3.6. Interchannel variability evaluation

In Section 3.4, CV was used to characterize the overall monodispersity of microdroplets generated within each device. In the same section, microdroplet generation frequency was also characterized for each device as a whole and the reported standard deviations only capture deviations between experimental replicates.

Here, we delve deeper into the performance of each individual channel within these devices, to reveal heterogeneity that can impact the reliability of high-throughput microdroplet production. Interchannel variability was evaluated in terms of both microdroplet generation frequency and microdroplet diameter using two interchannel coefficients of variation: $CV_{ch,f}$ and $CV_{ch,d}$. To maintain consistency and allow comparison to previous sections, experiments were conducted using the same Φs, i.e., 0.5, 1, 3, and 9, and identical flow rates. We found that $CV_{ch,d}$ follows a similar overall trend as the device-level microdroplet size CV, as it remains below 10% under most conditions, except for 30:30 and 180:20 μL/min for the Lateral-PFFD, and 10:10, 30:30, 18:6, and 60:20 μL/min for the Vertical-PFFD (Figure S8). As discussed in Section 3.4, these flow rates correspond to transitional regimes and the consistency between CV and $CV_{ch,d}$ indicates that intra-channel and inter-channel microdroplet size variability originate from the same hydrodynamic factors.

$CV_{ch,f}$ also remains below 10% for most tested conditions (Fig. 7, red horizontal lines). Similar to $CV_{ch,d}$, occasional spikes are observed at specific flow rate combinations. However, unlike $CV_{ch,d}$, these spikes ($CV_{ch,f}$>10%) do not coincide with transitional regimes, but are rather observed randomly and only when the dispersed phase flow rate is 10 μL/min or lower, suggesting that they are driven by refill-limited conditions [35]. This behavior aligns with the scaling relationships discussed in Section 3.5, which show that microdroplet diameter is primarily governed by Ca_c and only weakly depends on flow rates, whereas, microdroplet generation frequency is sensitive to Q_d. When comparing the two architectures, the Lateral-PFFD exhibits fewer spikes of $CV_{ch,f}$> 10% (one at 27:3 μL/min) compared to the Vertical-PFFD (four spikes at 10:10, 30:10, 27:3, and 90:10 μL/min). This empirical observation is again consistent with their fitted scaling parameters, specifically the exponent of Φ, which is much smaller (-0.03) for the Lateral-PFFD indicating weak sensitivity to flow rate imbalance, compared to −0.22 for the Vertical-PFFD indicating stronger dependence on flow conditions.

3.7. Comparative summary

To provide a concise overview of our experimental findings for the two PFFDs and facilitate comparison, their key application-relevant characteristics are summarized in Table 1 and compared across operational stability, microdroplet generation, inter-channel uniformity, and scalability. In terms of overall performance, the Lateral-PFFD is the "robust workhorse" as it offers a wider dripping regime, a broad monodispersity range (CV<10%), very low inter-channel variability, and hydrodynamically damped behavior, making it easier to operate stably over long periods. The Vertical-PFFD is the "high-performance specialist" as it generates smaller microdroplets under similar flow

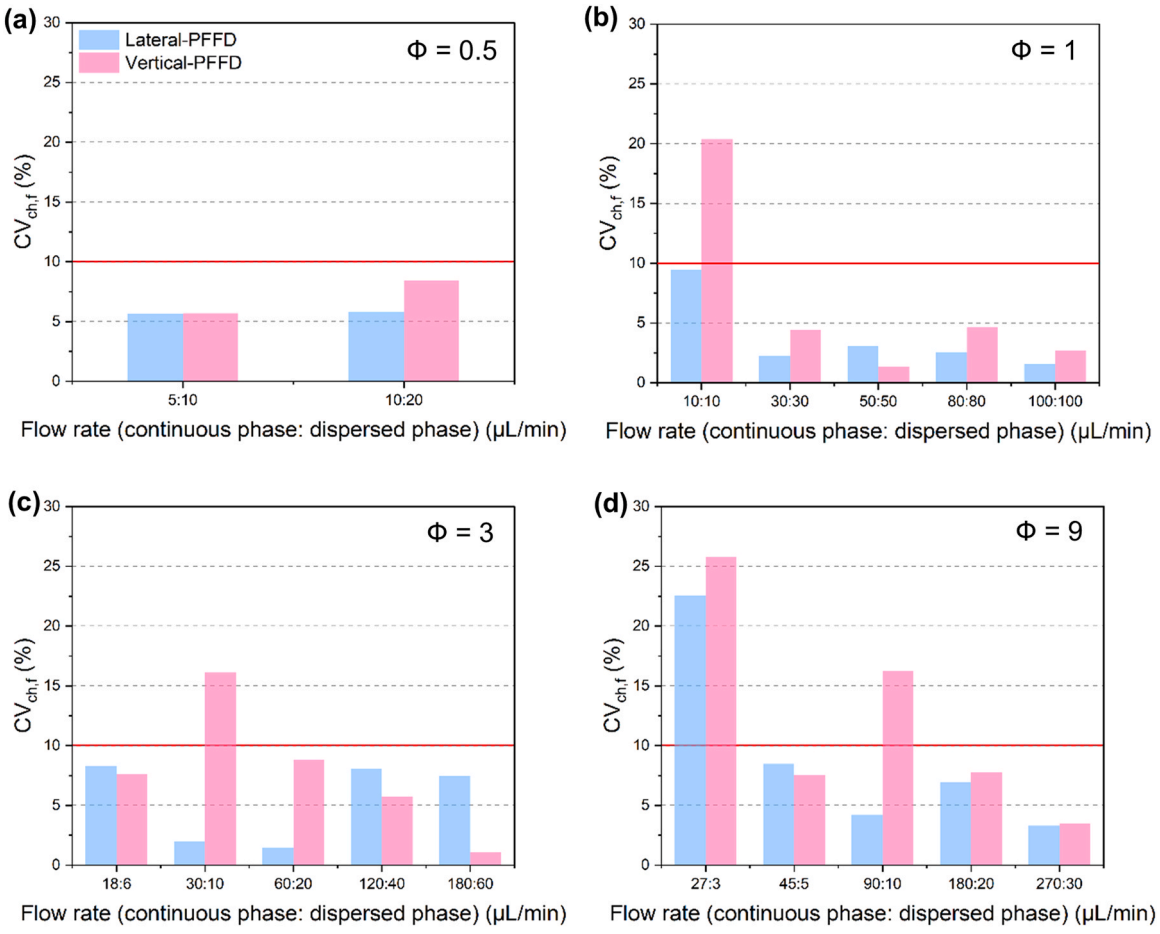

Fig. 7. Interchannel variability of microdroplet generation frequency ($CV_{ch,f}$) in Lateral-PFFD and Vertical-PFFD at (a) Φ= 0.5, (b) Φ= 1, (c) Φ= 3, and (d) Φ= 9. For each flow rate ratio, multiple total flow rates (μL/min) were tested. The red lines indicate $CV_{ch,f}$= 10%. Frequency desynchronization between channels appears randomly and only when $Q_d \leq$ 10 μL/min, as the system becomes refill-limited and more sensitive to flow partitioning.

Table 1
Comparison between the Lateral-PFFD and Vertical-PFFD in terms of operational stability, microdroplet generation, inter-channel uniformity, and scalability.

Aspect	Lateral-PFFD	Vertical-PFFD
Operational regime	Wide dripping regime	Narrower dripping range; more jetting
Microdroplet size	Larger at high flow rates	Smaller at high flow rates
Generation frequency	High, but lower that Vertical-PFFD	High
Monodispersity range (CV<10%)	Wide range of flow rates	Moderate range of flow rates
Sensitivity to Φ and Ca_a	Weak dependence	Stronger dependence
Interchannel variability	Very low	Noticeable at low Q_d (< 10 μL/min)
Hydrodynamic behavior	Damped shear and delayed pressure transmission	Fast pressure response, stronger local shear
Fabrication scalability	High flexibility, limited by lateral space	Limited by layer stacking and alignment
Best suited for	Parallel synthesis, bioassays, stable long-term operation	High-throughput emulsification
Overall characteristics	Robust, uniform	Fast, efficient

conditions and reaches higher frequencies, however, within a narrower dripping window and with a higher tendency toward jetting and desynchronization at low dispersed phase flow rates.

In terms of stability and uniformity, the performance of the Lateral-PFFD is only weakly affected by variations in flow rate ratio and capillary number, which results in a wide monodisperse window and very low channel-to-channel variability. This behavior arises from shear damping and delayed pressure transmission in the lateral architecture, which smooth short-term fluctuations and promote uniform microdroplet formation across outlets. By contrast, the Vertical-PFFD shows a stronger dependence on operating parameters, leading to increased interchannel variability and the need for tighter flow control. On the other hand, the vertical supply yields fast pressure response and stronger local shear, which boosts frequency and reduces microdroplet size but also makes the system more sensitive to imbalance.

When considering scalability and practical implementation, the Lateral-PFFDs can be scaled simply by adding more units laterally on the wafer, so throughput is mainly limited by planar area rather than by fabrication complexity. In contrast, scaling the Vertical-PFFDs is constrained by the maximum cutting depth (for wafer-based fabrication) and alignment tolerances, so only a limited number of vertical layers is feasible, making further scaling more fabrication-intensive. From a device design perspective, scaling the Vertical-PFFD architecture by adding more mDGUs also necessitates corresponding modifications to the main feed-channel configuration to preserve uniform flow distribution and minimize pressure losses. Because the Vertical-PFFD relies on multiple vertically stacked flow paths, maintaining equal hydraulic resistance across all layers becomes increasingly critical as the number of units grows, as discussed in **Section 3.1**.

In terms of operation and output, increasing the number of mDGUs would primarily influence the distribution of flow among the individual mDGU rather than the underlying droplet-formation mechanisms. As additional units are introduced, the total flow supplied to the device would be partitioned across a larger number of mDGUs, effectively reducing the flow rate delivered to each generator. As a result, the absolute operating flow rates required to achieve a given droplet size or generation frequency may shift. However, the overall architectural trends observed in this work, such as the higher achievable frequencies in the Vertical-PFFD and the wider monodisperse operating window of the Lateral-PFFD, are expected to remain unchanged, as they stem from the intrinsic hydrodynamic characteristics of the two geometries.

In summary, the Lateral-PFFD would be best positioned for parallel synthesis, bioassays, and other applications that prioritize stable, uniform, and easily scalable operation. The Vertical-PFFD is better suited to high-throughput emulsification, where achieving small microdroplets at high frequency justifies tighter control and more complex fabrication.

Having presented a direct head-to-head comparison between the lateral and vertical parallelized microfluidic devices studied here, we next consider how these results could be generalized to provide performance estimations in other similar parallelized systems. To establish such generalized performance estimations, direct comparison to existing work in the literature would be key. However, appropriate benchmarking via literature comparison is not feasible, as existing studies do not employ equivalent device architectures and operating conditions, nor directly contrast lateral and vertical parallelized microdroplet generators. Nevertheless, previous studies on ladder-type parallelization architectures provide useful context at the level of hydrodynamic design principles [36]. Although ladder architectures are most commonly implemented in planar geometries rather than in fully 3D vertical architectures, they share an important characteristic of the vertical architecture employed herein: the hydrodynamic resistance of the main supply channels is designed to be smaller compared to that of the individual mDGU. Under these conditions variations in the global distribution network have a reduced influence on the local driving conditions at each generator, resulting in more uniform operation across the array. The literature further identifies several system-level characteristics of ladder-type architectures in comparison to lateral parallelization schemes. In particular, ladder architectures generally require a smaller device footprint for a given number of generators, and their flow distribution is less sensitive to geometric variability or partial clogging. This reduced sensitivity arises because perturbations in a single generator primarily affect the local flow resistance and have only a limited influence on the flow supplied to the remaining units through the low-resistance manifold [17,37].

Taken together, the comparison presented here highlights key differences between lateral and vertical parallelized microfluidic droplet generation architectures within a consistent experimental framework. While direct quantitative comparison with prior literature is limited by differences in device geometry and implementation, relevant design principles from related parallelization strategies provide useful context for interpreting the observed trends.

4. Conclusions and future perspectives

In this study, we performed a systematic head-to-head comparison of two parallelized microdroplet generation architectures, the Lateral-PFFD and the Vertical-PFFD, to investigate how the geometric arrangement of mDGUs affects scalability, throughput, and microdroplet monodispersity. While both parallelization approaches have been widely used for microdroplet scale-up, previous work primarily focused on increasing overall throughput by implementing an ever-increasing amount of mDGUs, without directly comparing vertical and lateral configurations under identical experimental conditions. Here, we present the first systematic comparison of these two architectures operated within an identical operational window, bridging a critical gap in literature. Our results provide a quantitative understanding of how, and to what extent, geometric configuration dictates microdroplet formation dynamics, uniformity, and scalability, offering guidance for the design of future parallelized microfluidic systems. More fundamentally, these results highlight how geometric arrangement modulates interfacial breakup regimes and the associated scaling behavior in parallelized flow-focusing systems.

In addition to the systematic performance comparison, the present work also provides simple semi-quantitative scaling descriptions for microdroplet generation frequency and microdroplet size, derived directly from experimental observations. These relationships summarize the dominant trends observed across both architectures and offer an intuitive way to interpret how operating conditions influence microdroplet formation. Although these scaling relationships are only directly applicable to devices identical to the ones used in this work, their derivation and implementation offers a tool that can be adapted to other

architectures for similar mechanistic understanding. Together, the head-to-head comparison and the accompanying scaling descriptions provide practical guidance for selecting and designing parallel microdroplet generators for applications such as high-throughput screening, continuous microreactor-based chemical synthesis, and encapsulation in pharmaceutical and biotechnological contexts.

More importantly, by elucidating geometry-dependent interfacial breakup mechanisms and scaling behavior, this study reframes parallelization in microdroplet microfluidics as a physics-informed engineering design problem rather than a purely empirical scale-up exercise. We expect that this design-oriented view will help translate laboratory-scale parallel flow-focusing demonstrations into robust and scalable microfluidic systems.

CRediT authorship contribution statement

Lanting Xiang: Writing – original draft, Visualization, Validation, Project administration, Methodology, Investigation, Formal analysis, Data curation, Conceptualization. **Yu Zou:** Validation, Investigation, Formal analysis, Data curation. **Yuanpeng Yu:** Validation, Investigation, Formal analysis, Data curation. **Hazal Kutluk:** Writing – review & editing, Conceptualization. **Amina Moss:** Writing – review & editing, Software. **Iordania Constantinou:** Writing – review & editing, Writing – original draft, Supervision, Resources, Project administration, Funding acquisition, Conceptualization.

Declaration of Competing Interest

The authors declare that they have no known competing financial interests or personal relationships that could have appeared to influence the work reported in this paper.

Acknowledgments

This work and L.X. were financially supported by the German Research Foundation (DFG), grant number 502287023. The authors acknowledge support from the Open Access Publication Funds of Technische Universität Braunschweig.

Appendix A. Supporting information

Supplementary data associated with this article can be found in the online version at doi:10.1016/j.colsurfa.2026.140587.

Data Availability

Data will be made available on request.

References

[1] A. Shahidian, M. Ghassemi, J. Mohammadi, M. Hashemi, Application of microfluidics in cancer treatment, in: Bio-Engineering Approaches to Cancer Diagnosis and Treatment, Elsevier, 2020, pp. 219–250, https://doi.org/10.1016/B978-0-12-817809-6.00009-1.
[2] L. Jiang, N.S. Korivi, Microfluidics: technologies and applications, in: Nanolithography, Elsevier, 2014, pp. 424–443, https://doi.org/10.1533/9780857098757.424.
[3] E. Taiedinejad, C. Bausch, J. Wittek, G. Gül, P. Erfle, N. Schwarz, M. Mozafari, M. Baßler, A. Dietzel, Diffusive micromixing combined with dynamic in situ laser scattering allows shedding light on lipid nanoparticle precipitation, Sci. Rep. 14 (2024) 24356, https://doi.org/10.1038/s41598-024-73721-0.
[4] T. Moragues, D. Arguijo, T. Beneyton, C. Modavi, K. Simutis, A.R. Abate, J.-C. Baret, A.J. deMello, D. Densmore, A.D. Griffiths, Droplet-based microfluidics, Nat. Rev. Methods Prim. 3 (2023) 32, https://doi.org/10.1038/s43586-023-00212-3.
[5] Q. Yu, X. Chen, Insights into the breaking and dynamic mixing of microemulsion (W/O) in the T-junction microchannel, Chaos Solitons Fractals 155 (2022) 111774, https://doi.org/10.1016/j.chaos.2021.111774.
[6] L. Mazutis, J. Gilbert, W.L. Ung, D.A. Weitz, A.D. Griffiths, J.A. Heyman, Single-cell analysis and sorting using droplet-based microfluidics, Nat. Protoc. 8 (2013) 870–891, https://doi.org/10.1038/nprot.2013.046.
[7] J.J. Agresti, E. Antipov, A.R. Abate, K. Ahn, A.C. Rowat, J.-C. Baret, M. Marquez, A. M. Klibanov, A.D. Griffiths, D.A. Weitz, Ultrahigh-throughput screening in drop-based microfluidics for directed evolution, Proc. Natl. Acad. Sci. 107 (2010) 4004–4009, https://doi.org/10.1073/pnas.0910781107.
[8] Y. Li, J. Zhang, L. Zhuo, X. Wang, J. Sun, P. Xue, K. Chen, Microfluidics-engineered microcapsules: advances in thermal energy storage and regulation, Micro (Basel) 16 (2025) 830, https://doi.org/10.3390/mi16070830.
[9] A. Ratanpara, Y. Li, M. Kim, A review of microfluidic approaches for carbon capture and storage research, Lab Chip 25 (2025) 5705–5746, https://doi.org/10.1039/D5LC00208G.
[10] H. Kutluk, M. Viefhues, I. Constantinou, Integrated microfluidics for single-cell separation and on-chip analysis: novel applications and recent advances, Small Sci. 4 (2024), https://doi.org/10.1002/smsc.202300206.
[11] Y. Ding, P.D. Howes, A.J. deMello, Recent advances in droplet microfluidics, Anal. Chem. 92 (2020) 132–149, https://doi.org/10.1021/acs.analchem.9b05047.
[12] S.G. Sontti, A. Atta, Regulation of droplet size and flow regime by geometrical confinement in a microfluidic flow-focusing device, Phys. Fluids 35 (2023), https://doi.org/10.1063/5.0130834.
[13] W. Han, X. Chen, A review on microdroplet generation in microfluidics, J. Braz. Soc. Mech. Sci. Eng. 43 (2021) 247, https://doi.org/10.1007/s40430-021-02971-0.
[14] T. Ward, M. Faivre, M. Abkarian, H.A. Stone, Microfluidic flow focusing: drop size and scaling in pressureversus flow-rate-driven pumping, Electrophoresis 26 (2005) 3716–3724, https://doi.org/10.1002/elps.200500173.
[15] W. Han, X. Chen, New insights into the pressure during the merged droplet formation in the squeezing time, Chem. Eng. Res. Des. 145 (2019) 213–225, https://doi.org/10.1016/j.cherd.2019.03.002.
[16] F. Mardani, S. Falahatian, M. Taghipoor, Mapping flow-focusing microfluidic droplet formation to determine high-throughput droplet generation configurations, Results Eng. 18 (2023) 101125, https://doi.org/10.1016/j.rineng.2023.101125.
[17] J. Wu, S. Yadavali, D. Lee, D.A. Issadore, Scaling up the throughput of microfluidic droplet-based materials synthesis: a review of recent progress and outlook, Appl. Phys. Rev. 8 (2021), https://doi.org/10.1063/5.0049897.
[18] D. Bardin, M.R. Kendall, P.A. Dayton, A.P. Lee, Parallel generation of uniform fine droplets at hundreds of kilohertz in a flow-focusing module, Biomicrofluidics 7 (2013), https://doi.org/10.1063/1.4811276.
[19] D. Monserrat Lopez, P. Rottmann, M. Fussenegger, E. Lörtscher, Silicon-based 3D microfluidics for parallelization of droplet generation, Micro (Basel) 14 (2023) 1289, https://doi.org/10.3390/mi14071289.
[20] D. Conchouso, D. Castro, S.A. Khan, I.G. Foulds, Three-dimensional parallelization of microfluidic droplet generators for a litre per hour volume production of single emulsions, Lab Chip 14 (2014) 3011, https://doi.org/10.1039/C4LC00379A.
[21] S. Yadavali, H.-H. Jeong, D. Lee, D. Issadore, Silicon and glass very large scale microfluidic droplet integration for terascale generation of polymer microparticles, Nat. Commun. 9 (2018) 1222, https://doi.org/10.1038/s41467-018-03515-2.
[22] Q. Yang, Z. Wang, Q. Gao, Y. Zhao, C. Jiang, Study of droplet formation in parallel flow focusing microchannel under electrostatic field control, Colloids Surf. A Physicochem. Eng. Asp. 695 (2024) 134174, https://doi.org/10.1016/j.colsurfa.2024.134174.
[23] T. Femmer, A. Jans, R. Eswein, N. Anwar, M. Moeller, M. Wessling, A.J.C. Kuehne, High-throughput generation of emulsions and microgels in parallelized microfluidic drop-makers prepared by rapid prototyping, ACS Appl. Mater. Interfaces 7 (2015) 12635–12638, https://doi.org/10.1021/acsami.5b03969.
[24] T. Kamperman, L.M. Teixeira, S.S. Salehi, G. Kerckhofs, Y. Guyot, M. Geven, L. Geris, D. Grijpma, S. Blanquer, J. Leijten, Engineering 3D parallelized microfluidic droplet generators with equal flow profiles by computational fluid dynamics and stereolithographic printing, Lab Chip 20 (2020) 490–495, https://doi.org/10.1039/C9LC00980A.
[25] M. Vigogne, T.A. Neuendorf, R. Bernhardt, J. Thiele, Combining parallelized emulsion formation and sequential droplet splitting for large-scale polymer microgel production, J. Polym. Sci. 61 (2023) 1902–1911, https://doi.org/10.1002/pol.20230213.
[26] J. Zhang, Q. Ji, H. Duan, Three-dimensional printed devices in droplet microfluidics, Micro (Basel) 10 (2019) 754, https://doi.org/10.3390/mi10110754.
[27] C. Chung, B. Cui, R. Song, X. Liu, X. Xu, S. Yao, Scalable production of monodisperse functional microspheres by multilayer parallelization of high aspect ratio microfluidic channels, Micro (Basel) 10 (2019) 592, https://doi.org/10.3390/mi10090592.
[28] L. Xiang, J. Solarczek, V. Krajka, H. Liu, L. Ahlborn, A. Schallmey, I. Constantinou, Evaluating the Potential of Microdroplet Flow in Two-Phase Biocatalysis: A Systematic Study, ACS Appl. Mater. Interfaces (2025), https://doi.org/10.1021/acsami.4c15647.
[29] H.H. Kim, Y. Cho, D. Baek, K.H. Rho, S.H. Park, S. Lee, Parallelization of microfluidic droplet junctions for ultraviscous fluids, Small 18 (2022), https://doi.org/10.1002/smll.202205001.
[30] M. Muluneh, D. Issadore, Hybrid soft-lithography/laser machined microchips for the parallel generation of droplets, Lab Chip 13 (2013) 4750, https://doi.org/10.1039/c3lc50979f.
[31] Z. Yin, Z. Huang, X. Lin, X. Gao, F. Bao, Droplet generation in a flow-focusing microfluidic device with external mechanical vibration, Micro (Basel) 11 (2020) 743, https://doi.org/10.3390/mi11080743.
[32] Y. Yang, J. Fu, K. Mu, S. Wang, P. Zhu, T. Si, Dynamics of droplet formation in rotary flow focusing, Flow 5 (2025) E34, https://doi.org/10.1017/flo.2025.10025.
[33] T. Ward, M. Faivre, M. Abkarian, H.A. Stone, Microfluidic flow focusing: Drop size and scaling in pressure versus flow-rate-driven pumping, Electrophoresis 26 (2005) 3716–3724, https://doi.org/10.1002/elps.200500173.

[34] L. Xiang, Y. Zou, Y. Yu, H. Kutluk, A. Moss, I. Constantinou, PFFD Scaling Operation Tool (Shiny app) for microdroplet parallelisation, Zenodo (2026), https://doi.org/10.5281/zenodo.18389993.
[35] A.M. Ibrahim, J.I. Padovani, R.T. Howe, Y.H. Anis, Modeling of droplet generation in a microfluidic flow-focusing junction for droplet size control, Micro (Basel) 12 (2021) 590, https://doi.org/10.3390/mi12060590.
[36] H.-H. Jeong, V.R. Yelleswarapu, S. Yadavali, D. Issadore, D. Lee, Kilo-scale droplet generation in three-dimensional monolithic elastomer device (3D MED), Lab Chip 15 (2015) 4387–4392, https://doi.org/10.1039/C5LC01025J.
[37] G. Tetradis-Meris, D. Rossetti, C. Pulido de Torres, R. Cao, G. Lian, R. Janes, Novel parallel integration of microfluidic device network for emulsion formation, Ind. Eng. Chem. Res. 48 (2009) 8881–8889, https://doi.org/10.1021/ie900165b.